Chapter 2
Imaging the Magnetic Near-Field of Plasmon Modes in Bar Antennas

Abstract In this chapter, we show how the scanning near-field optical microscopy (SNOM) technique can be used to visualize the lateral magnetic near-fields of metallic nanostructures, namely gold bars. We present direct experimental maps of these fields by using hollow-pyramid aperture probe SNOM. The results are supported by numerical simulations in which we first simulate the fields of the probe and the bars separately. Then we simulate and discuss in details how the probe-sample interaction results in the effective formation of a lateral magnetic dipole. This allows obtaining optical contrast in the SNOM images corresponding to the lateral magnetic near-fields of the structures. We verify the results for different bar lengths and wavelengths, respectively different plasmon modes. The obtained specific relation of the bar length versus resonant wavelength (so called dispersion relation), allows to unambiguously confirm that the observed optical contrast is related to plasmonic effects.

2.1 Introduction

As discussed in Chap. 1, photonic nanomaterials, and in particular plasmonic nanoantennas, enable light [1–5] and matter [6] manipulation at the nanoscale. Many of the newly emerging fields in photonics are relying on plasmonic devices as essential building blocks, for example—all-optical signal processing devices [7–11], metamaterials [12, 13], ultrahigh sensitivity bio- and chemical- sensors [14–18], and active photodetectors [19, 20], to name a few.

One of the key factors determining the functionality of these photonic devices is the local distribution of the electric and magnetic field components in the vicinity of the nanostructures' boundaries. As mentioned in the introduction, in metamaterials for example, both the electric [21] and the magnetic [22] interactions between the artificial atoms play a crucial role in obtaining negative permittivity and negative

The results presented in this chapter are based on and reproduced with permission from:
D. Denkova, N. Verellen, A.V. Silhanek, V.K. Valev, P. Van Dorpe, V.V. Moshchalkov
Mapping magnetic near-field distributions of plasmonic nanoantennas
ACS Nano **7**, 3168 (2013). Copyright © 2013, American Chemical Society.

© Springer International Publishing Switzerland 2016

D. Denkova, *Optical Characterization of Plasmonic Nanostructures: Near-Field Imaging of the Magnetic Field of Light*, Springer Theses, DOI 10.1007/978-3-319-28793-5_2

permeability, which are necessary for the design and the engineering of, e.g., optical cloaking [23] and negative refractive index materials [13, 24]. Recently, a lot of efforts have been concentrated on achieving magnetic field enhancement at optical frequencies [25–27] with prospective applications [28], for example, as magnetic sensors [29, 30] and for achieving magnetic non-linear effects [31]. Therefore, both from fundamental science and applications point of view, mapping not only the electric but also magnetic near-field distributions has become of crucial importance.

Realizing that with standard far-field optical microscopy methods is impossible, as they have insufficient resolution and provide no information about the electromagnetic near-fields [32, 33]. In recent years, several techniques—each with its own specific scope, advantages and restrictions—have been developed and optimized to gain access to the optical near-fields, *e.g.*: cathodoluminescence (CL) [34], electron energy-loss spectroscopy (EELS) [35], two photon luminescence (TPL) [36], second harmonic generation (SHG) microscopy [6], and scanning near-field optical microscopy (SNOM) [29, 37–39].

In this thesis, we focus on the SNOM technique [40, 41]. It relies on scanning different types of probes in the near-field of a sample, which allows imaging different components of the electromagnetic near-field. For example, the vertical electric field component (relative to the sample surface) can be mapped by the sharp needle of a scattering-SNOM [42, 43]. On the other hand, images obtained with a metal coated optical fiber probe, having a sub-wavelength hole at its apex (aperture-SNOM), have been interpreted in terms of local density of optical states (LDOS) [38, 44, 45], magnetic field [30, 46], or lateral electric field [47, 48]. However, no consensus has been reached regarding the image interpretation and the obtained results might be sensitive to small variations in the probe structure and geometry.

While imaging of the electric field components is nowadays considered a standard procedure, mapping of the much more weakly interacting magnetic field components [49] remains a challenging non-trivial task. Indirect procedures have been explored, relying on the calculation of the magnetic field components from the electric field components via Maxwell's equations [50–53]. However, direct measurements of the magnetic field at optical frequencies remain difficult. Significant progress in this direction has been reported by Burresi et al. [29], who have developed a special split-ring like probe for mapping the *vertical magnetic* field component.

Instead, here we demonstrate mapping of the *lateral magnetic* near-field distribution of different plasmon modes in metallic bars, by a hollow-pyramid probe aperture-SNOM (Fig. 2.1a). This type of probes has been used, for instance, for investigating propagating surface plasmon polaritons (SPP) [5, 39, 54, 55]. In these studies, however, the probe-sample coupling and the image contrast formation mechanism, which are crucial for understanding light confining effects in nanoantennas, have not been addressed in details. In this chapter, we propose such a mechanism and illustrate how it effectively results in mapping of the lateral magnetic field distribution of plasmonic nanoantennas.

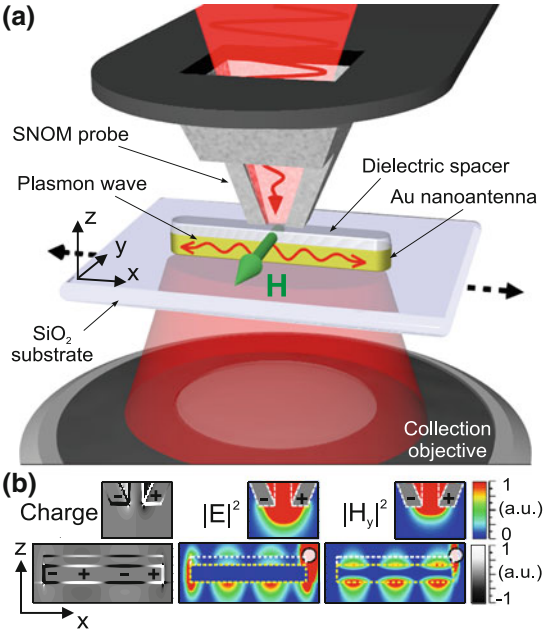

Fig. 2.1 Near-field scanning of a plasmonic nanoantenna with a hollow-pyramid probe. **a** Schematics of the transmission SNOM setup. Electromagnetic coupling between the Al coated hollow-pyramid SNOM probe and the gold nanoantenna induces a lateral magnetic dipole and can excite surface plasmon resonances (SPRs) in the bar. By detecting the transmitted light intensity, while scanning the sample, this dipole allows mapping of SPR magnetic field anti-nodes. **b** Charge density, electric and magnetic field distributions. *Top* at the probe aperture for an x-polarized incident plane wave at $\lambda = 1\,\mu$m. *Bottom* for the $l = 3$ SPR antenna mode ($\lambda = 1270$ nm), excited via an x-polarized dipole source, indicated with the *white circle*. Dimensions of the nanobar are: length $L = 1120$ nm, width $W = 70$ nm and height $h = 50$ nm. The thickness of the dielectric spacer is 30 nm. x-z cross-sections are taken through the probe/sample center

2.2 Results and Discussion

Near-field measurements are performed with a commercial SNOM system—WITec, alpha300 S [56]. The concept of the experiment is illustrated in Fig. 2.1a and a detailed description of the setup is given in Sect. 1.3.3. In short, polarized monochromatic light is focused on the apex of a SNOM probe. This probe consists of a hollow SiO_2 pyramid, mounted on an atomic force microscopy (AFM) cantilever. The pyramid is coated with a 100 nm thick Al layer, which is etched through at the apex. This opens up an aperture with a sub-wavelength diameter of nominally 100 nm, which provides optical resolution below the diffraction limit. For clarity, in Fig. 2.1a, the pyramid is partially cut open.

A part of the incident light can tunnel through the aperture and interact with the sample. The transmitted light is then collected and sent to the detector. Excitation and detection axes are kept collinear while the sample is being scanned in AFM contact mode underneath the probe.

2.2.1 Individual Probe and Sample Characterization

The detected image contrast is a result from the coupling between the near-fields of the probe and the respective near-fields of the sample. Therefore, we first performed a separate study of the probe and the sample. Finite-difference time-domain (FDTD) simulations of the probe reveal that an incident polarized plane wave induces a dipolar charge polarization at its apex—indicated with "+" and "−" signs in Fig. 2.1b, top. This leads to concentration of the electric and magnetic fields, as illustrated for $|E|^2$ and $|H_y|^2$. Due to symmetry considerations, the latter is the only non-zero magnetic field component in the provided x-z cross-section, through the middle of the probe.

All field components, as well as the charge and current density, near the probe aperture are given in the Methods Sect. 2.4, Fig. 2.8. The profiles are obtained at $\lambda = 1\,\mu$m and remain almost unchanged throughout the experimental spectral range. Details on the performed simulations can be found in the Methods Sect. 2.4.

The nanoantenna structure consists of a 50 nm thick and 70 nm wide gold nanobar, covered by a 30 nm thick dielectric layer (see Methods Sect. 2.4, Fig. 2.7). This layer enables scanning of the sample in contact mode while preventing strong conductive coupling between the probe and the sample.

When such a nanobar is illuminated with light, polarized along its long axis, charge density waves at the surface of the metal are excited. They can form standing wave-like Fabry-Pérot resonances, known as surface plasmon resonances (SPRs) [57]. Here, the resonance mode index l is defined as the number of half plasmon wavelengths $\lambda_p/2$ that fit the antenna cavity at resonance.

At positions with high charge density in the bar, strong enhancement of the electric near-field occurs and complementary magnetic maxima appear. This is illustrated in the simulation shown in Fig. 2.1b (bottom) for the $l = 3$ SPR mode, where the mode index is identified from the presented near-field profiles. Here, the antenna is excited by an x-polarized electric dipole, indicated with the white circle. Again, it is worth noticing that H_x and H_z are zero in the central x-z cross-section, as a result of the system's symmetry. Furthermore, the excitation of an SPR leads to resonant enhancement of the antenna's absorption and scattering cross-sections.

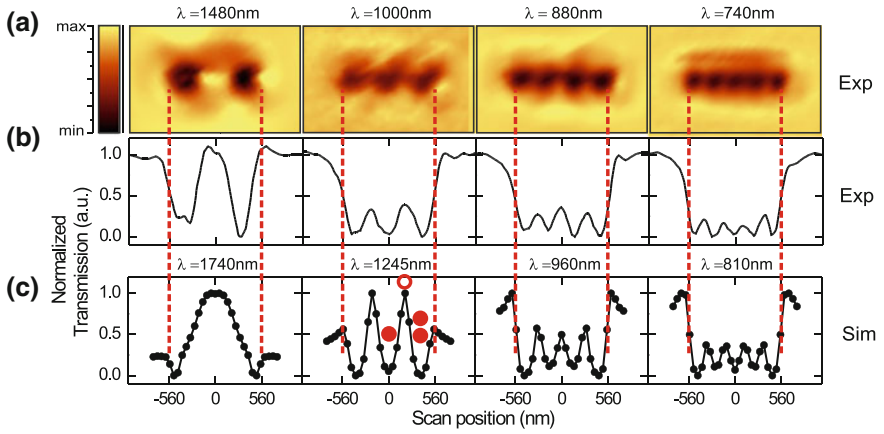

Fig. 2.2 Experimental and simulated near-field transmission scans. **a** Experimental SNOM maps of a nanobar antenna with $L = 1120$ nm at different wavelengths. *Dark* regions indicate reduced transmission intensity. **b** Normalized line scans of the maps in panel a through the center of the antenna. **c** Simulations reproducing the experimental data from panel b. *Red dashed lines* indicate the antenna borders. *Red dots* and *circles* refer to the probe positions, discussed in Fig. 2.3

2.2.2 *Probe-Sample Coupling: Imaging of the $|H_y|^2$ Near-Field Distribution of an $l = 3$ Plasmon Mode in a Gold Bar*

Now that the sample and probe have been characterized individually, the near-fields induced at the apex of the probe can be used to locally excite SPRs in the near-field region of the nanoantenna.

Experimental near-field scans of a single antenna with length $L = 1120$ nm measured at different excitation wavelengths are shown in Fig. 2.2a. Normalized line scans from the maps in panel a, taken through the center of the bar, are shown in panel b. For each mode, the baseline was subtracted in order to set the transmission minimum to zero, after which the data was normalized to the transmission intensity at the substrate to account for the wavelength dependence of the probe's transmittance [58]. This normalization is chosen to optimize the image contrast, at the expense of losing the absolute transmission intensity information. The light transmitted by the probe is not fully suppressed (*i.e.* not reaching zero) at the transmission minima. Since the nanoantenna is optically thin and narrower than the probe aperture, in addition to the finite extinction cross-section of the SPR resonances, a certain amount of light still reaches the detector. The outer boundaries of the bar are indicated with dashed lines.

Well defined dark spots corresponding to suppressed transmission are observed, while the number of dark spots increases towards shorter wavelengths of the excitation light. From left to right, the strongest transmission contrast was obtained at λ = 1480, 1000, 880 and 740 nm, respectively. For an accurate determination of these

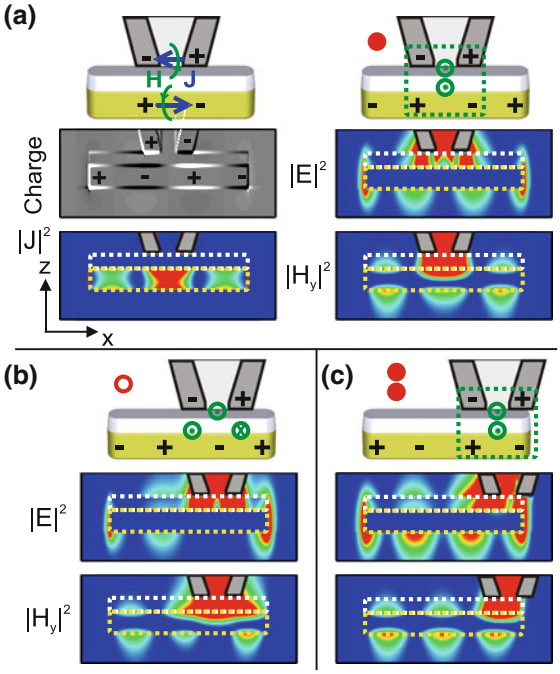

Fig. 2.3 Probe-antenna coupling leads to efficient excitation of SPR only at the lateral magnetic field maxima. **a** *Top* Illustration of image charge formation, induced current J and magnetic field H. *Bottom* simulated charge, current density, $|E|^2$ and $|H_y|^2$ profiles in x-z plane through the middle of the probe and antenna at $\lambda = 1245$ nm with probe at the center of the bar. **b** Simulated $|E|^2$ and $|H_y|^2$ profiles under the same conditions as (**a**), but with probe positioned at 200 nm from the center and **c** near the edge of the antenna. "+" and "−" indicate positive and negative charge accumulation, respectively. *Green circles* indicate out-of-plane magnetic field concentration. In the different panels $|E|^2$ and $|H_y|^2$ profiles have the same color scale, respectively. *Red dots* and *circles* are indicating the position of the tip, shown in Fig. 2.2c. For clarity, the schematic images are not to scale

resonant wavelengths, near-field maps were taken in steps of $\Delta\lambda = 20$ nm and compared. The characteristic features of the experimental near-field images are similar to those of the simulated SPR near-field profiles in Fig. 2.1b and to previous reports with scattering- and optical fiber aperture-SNOM on nanorods [37, 38, 59].

The exact relation between the transmission contrast and SPR near-field distribution is, however, not straightforward and one has to be careful with the interpretation of the SNOM images. We therefore performed extended simulations, including the probe-sample interaction, to reproduce the experimental maps and elucidate the contrast formation mechanisms.

The simulated transmission scans corresponding to Fig. 2.2b taken at, from left to right, $\lambda = 1740$, 1245, 960, and 810 nm, are shown in panel c. These curves were obtained by scanning the probe in 50 nm steps across the antenna while collecting the transmitted light intensity through an area spanning the same angle as the numerical

aperture (NA) of the objective in the measurement. The simulated scans accurately reproduce the experimental number of transmission minima and their relative positions.

The spectral shifts observed between the experimental (panels a and b) and simulated (panel c) transmission resonances most likely originate from deviations from the ideal sample and probe geometry (dimensions, shape, surface roughness, grain boundaries), as well as their optical material properties (depending on fabrication process), used in the simulations. As these parameters are hard to control and accurately determine experimentally, it is difficult to avoid such a spectral mismatch.

We can now confidently use the full-field three dimensional simulations to investigate how the probe fields excite surface plasmons in the nanoantenna, and how this excitation influences the detected transmission intensity. Figure 2.3 provides a more in-depth analysis for the case where three transmission minima are observed in Fig. 2.2c ($\lambda = 1245\,\text{nm}$) and the probe is located at the same positions as those indicated with red dots and the open circle. In Fig. 2.3a, the probe is positioned above the antenna center and the top left panel illustrates how the polarized charges at the rim of the probe generate image charges in the metallic nanostructure.

This effect is evidenced by the strong electric field intensity $|E|^2$ observed between the Al coating of the probe (grey areas) and the nanobar (also seen in Fig. 2.3b, c). This anti-parallel dipole coupling effectively generates an out-of-plane y-oriented magnetic dipole (green arrows in Figs. 2.1a and 2.3) [60, 61]. The strong lateral magnetic field enhancement is clearly observed in the corresponding $|H_y|^2$ field profiles.

The charge separation induced by the probe, disturbs the free electron gas in the antenna and launches a surface plasmon wave. Even when driven at one of the SPR frequencies, the probe couples to an SPR only at positions for which the waves, reflected back from the antenna edges, are phase matched to form a standing wave pattern. These positions are exactly the nodes in the corresponding SPR charge density distribution.

The charge distribution in Fig. 2.3a clearly shows the standing wave pattern expected for the $l = 3$ antenna mode, exhibiting three charge nodes and *four anti-nodes in the electric field profile*. This resonant charge oscillation translates into three regions of high current density $|J|$ and consequently, through Ampère's law, *three magnetic field anti-nodes*. The top right panel of Fig. 2.3a illustrates how the charges and magnetic near-field (green circles) at the probe aperture line up with the charge distribution and magnetic near-field of the SPR mode.

When resonantly excited, both the absorption and scattering cross-sections of the nanoantenna are drastically enhanced. This means that part of the power transmitted by the probe is absorbed and redirected by the antenna, resulting in a lower detected signal, and therefore, a dark spot in the SNOM image (Fig. 2.2c, single red dot).

When the probe is gradually moved off-center, the symmetric standing wave profile, clearly seen in the $|E|^2$ and $|H_y|^2$ profiles at the bottom surface of the nanobar, is disturbed. Up to a point where one of the four electric field maxima, characteristic for the $l = 3$ mode, disappears. This situation is shown in Fig. 2.3b where the probe is shifted 200 nm from the bar's center. Here, no efficient coupling between the different

electric and magnetic field components occurs and excitation of the $l = 3$ mode is not expected. The open red circle in Fig. 2.2c indicates that this results in a transmission maximum.

When approaching the antenna edge (Fig. 2.3c), however, the next $l = 3$ SPR magnetic anti-node is probed. The symmetric SPR field profiles are restored and another transmission minimum is detected (Fig. 2.2c, double red dot).

The closer the probe is to the maximum of the antenna's magnetic field, the stronger the resulting out-of-plane coupled magnetic dipole becomes, leading to stronger excitation of the SPR mode. Consequently, more light is absorbed and less light reaches the detector. From this analysis we can conclude that the SPR field component, effectively mapped in this type of near-field measurement, is H_y.

To further illustrate that the experimental maps indeed correspond to the $|H_y|^2$ field profiles, a comparison between the measured SNOM map and the different components of the electromagnetic near-field of the nanobar is shown in Fig. 2.4. For the simulation, the surface plasmon resonance in the antenna is excited with a dipole source, positioned above one end of the antenna. The profiles are taken at the resonant wavelength for the $l = 3$ SPR mode ($\lambda = 1270$ nm). The electric field components have a common color scale. The magnetic field components also have a common scale bar, except $|H_x|^2$ for which the maximum intensity is an order of magnitude lower.

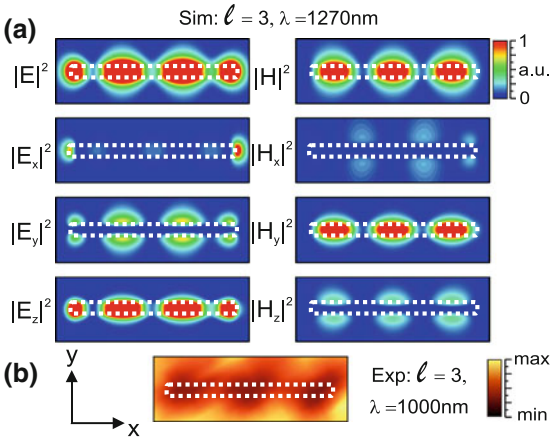

Fig. 2.4 **a** Electric (*left*) and magnetic (*right*) field distributions for a gold nanobar with $L = 1120$ nm for the $l = 3$ SPR mode ($\lambda = 1270$ nm). x-y cross-sections are taken at 30 nm from the gold top surface. **b** Experimental transmission map for the same mode reproduces the $|H_y|^2$ distribution. The *white boxes* outline the nanobar

2.2.3 Imaging of the $|H_y|^2$ Near-Field Distribution of Different Plasmon Modes in a Gold Bar

Since a transmission minimum was shown to correspond to a region with enhanced magnetic field, it is now possible to unambiguously assign the proper mode index l to the different SPR modes seen in the SNOM maps of Fig. 2.2.

Clearly, the experimental near-field maps reproduce the calculated magnetic field maxima for the $l = 2$, 3, 4, and 5 antenna modes, as illustrated in Fig. 2.5. It is interesting to note that even order modes are also detected [14]. The localized excitation of SPRs offers the necessary symmetry reduction to excite these otherwise dark modes. The simulated profiles here are also obtained by placing a dipole source above one end of the antenna to introduce the phase retardation, which however, leads to a small asymmetry seen in the profiles. From a comparison of the simulation with (Fig. 2.2c) and without (Fig. 2.5 bottom row) the SNOM probe, it can be concluded that the presence of the probe in the near-field of the sample leads to a slight blue-shift of a few percent of the resonant wavelengths. Spectral shifts on the same order of magnitude were observed in other SNOM studies using different types of metal coated and non-metallic probes [62, 63].

2.2.4 Plasmon Dispersion Relation Obtained by SNOM

A typical near-field scan of a nanoantenna array of increasing length L is shown in Fig. 2.6a. Following the dashed arrows, L varies from $L = 720$ nm in the top left to $L = 1800$ nm in the bottom right corner. The width and the height of the bars are kept constant—respectively $W = 70$ nm and $h = 50$ nm. The scan was performed in contact mode at a wavelength of 1100 nm. As L increases, additional half SPP wavelengths can fit the antenna cavity, higher order SPR modes are excited and the number of transmission minima increases (Fig. 2.6).

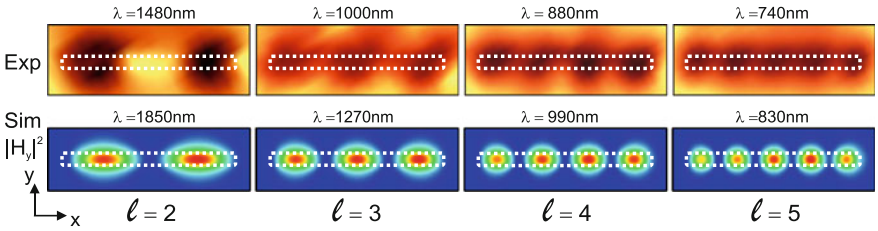

Fig. 2.5 Experimental SNOM transmission maps reproduce the simulated SPR lateral magnetic near-field distributions. Experimental transmission minima seen in Fig. 2.2a, zoomed in in the *top row* here, correspond to the simulated *magnetic near-field maxima* of the $l = 2$, 3, 4, and 5 SPR modes in the nanobar antenna ($L = 1120$ nm), shown in the *bottom row*. Field profiles are taken at 30 nm from the antenna surface. The *white boxes* outline the nanobar

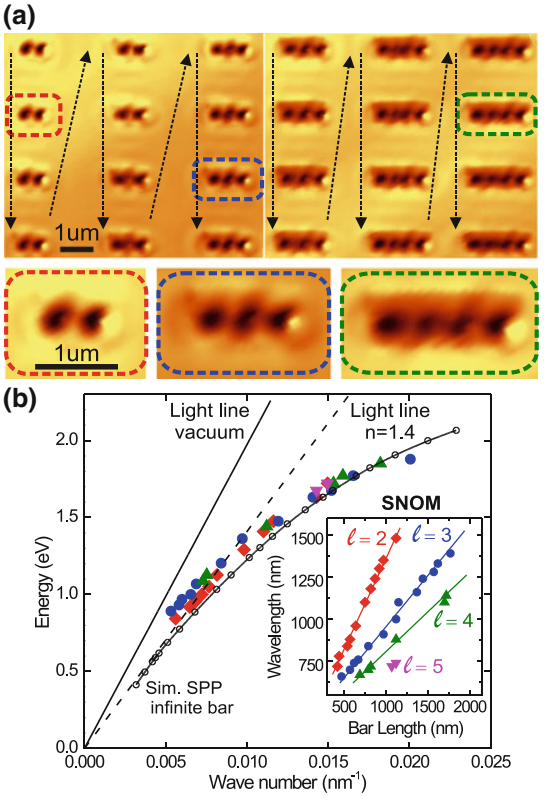

Fig. 2.6 Dispersion relation confirms that SNOM results are related to plasmonic effects. **a** Experimental SNOM scans at $\lambda = 1100$ nm and polarization along the bars' axis of two arrays with bars of increasing length (indicated by the *dashed arrows*). Zoomed in bars with resonant transmission contrast are shown in the *bottom panels*. $L = 750$, 1150 and 1700 nm from *left* to *right*, respectively. **b** Dispersion curves showing resonant plasmon energy versus plasmon wave number k defined as $k = \pi l/L$. Closed symbols: experimental near-field transmission resonances for $l = 2$, 3, 4, and 5 modes. *Solid* and *dashed lines* show the *light line* in vacuum and in n = 1.4 medium, resp. Black circles: calculated plasmon dispersion of an antenna of infinite length L. Inset: the dispersion data displayed as $\lambda(L)$ illustrates the expected linear wavelength scaling behavior for metallic nanorod antennas

Since the SPR modes are spectrally relatively broad, several antennas show the same number of dark transmission spots at a fixed wavelength. To define the resonant antenna length, for a specific SPR mode, again the bar showing the strongest transmission contrast for a line scan through the middle of the bar, was chosen. The resonant antennas in Fig. 2.6a are indicated with dashed boxes and have a length of L = 750, 1150 and 1700 nm from left to right, respectively. Note that the systematically observed gradual transition between the plasmon modes excludes possible sample imperfections as the origin of the image contrast and thus, such imperfections, if present, do not affect the presented data analysis and conclusions.

Performing this measurement at different wavelengths allows to map out the SPR dispersion curve, as shown in Fig. 2.6b (closed symbols). The SPR wave number $k = 2\pi/\lambda_p$, with λ_p the SPR wavelength, is defined as $k = \pi l/L$, resulting from the geometrical condition of a standing wave in the antenna cavity [38]. Here, L is the antenna length and l the mode index which was demonstrated to correspond to the number of transmission dips. In defining k a possible systematic error resulting from the non-trivial phase shift of the plasmon wave upon reflection at the bar edges is ignored. This phase shift is introduced by the complex refractive index of the dispersive metallic medium of the plasmon wave [34, 38]. After measuring all points, the first few points and a few random points were remeasured to exclude possible resonance shifts caused by wearing out of the tip.

The solid and dashed lines in Fig. 2.6b are the light lines in vacuum and in a glass medium, with refractive index $n = 1.4$, respectively. Open circles represent the calculated mode dispersion of propagating SPP in the nanoantenna geometry with infinite length L (see Methods Sect. 2.4).

Both the experimental cavity mode dispersion and calculated SPP dispersion bend to the right of the light line at larger wave numbers illustrating the sub-wavelength nature of surface plasmons. This excellent agreement between the dispersion curves further demonstrates that the experimentally observed near-field transmission contrast is indeed mapping plasmonic modes in the nanobar antennas and so justifies the standing wave description [64].

The inset in Fig. 2.6b shows the dispersion data as wavelength *versus* bar length. This graph further illustrates the expected linear wavelength scaling behaviour for metallic nanorod antennas [65–67].

Finally, the presented results can be situated among other reported techniques for obtaining the magnetic field of light. As already pointed out in the introduction, several methods to calculate the magnetic field from the electric field via Maxwell's equations have been developed in the terahertz [52, 53] and optical frequency regions [50, 51]. Although this approach has the advantage of providing information on both the electric and magnetic field components simultaneously (including their phase) it remains as an indirect method which requires post-processing of the data.

One of the most direct ways to measure the optical magnetic field is based on a split ring probe [29]. This is also a phase sensitive method with, in principle, no restrictions concerning the type of optical waves under investigation. However, it has the disadvantage that such probes are not commercially available and they can only access the vertical component of the magnetic field.

Devaux et al. [46] have reported that excitation of resonant circular plasmons in metalized aperture probes can lead to imaging of the magnetic field intensity in dielectric samples. The method is based on resonant effects in the probe and is therefore strongly restricted in terms of illumination wavelength. Another method, allowing simultaneous imaging of the vertical magnetic and electric field components in photonic crystal cavities has recently been reported [68, 69]. It is based on a particular blue-shift induced in the resonant frequencies of those samples and its applicability to other photonic (including plasmonic) systems has not been demonstrated so far.

Most notably, in contrast to the methods mentioned above, the technique we propose here provides information about the *lateral* magnetic field distribution in plasmonic antennas. Our measurements use commercially available probes and do not involve any additional data processing. Moreover, we expect our results to be directly applicable to the more widely used metal coated optical fiber probes, as their geometry is very similar to the one of the hollow-pyramid probes, used in this study. Indications that the metal coated optical fiber probes might indeed be sensitive to the magnetic near-field have been reported [30, 46]. Compared to the optical fiber, the hollow-pyramid probes are very robust [70] (we have experienced that a probe can easily provide good quality images for more than 2–3 months). The probes allow measurements in a broad wavelength region, in our case 500–1600 nm, the limitations coming from the excitation sources and the detectors. As of today, our microscope is not equipped to perform phase-sensitive measurements, but this could be implemented.

It should be emphasized that the presented in this chapter results only demonstrate the applicability of the technique to plasmonic waves in metallic nanobar antennas. Nevertheless, imaging of the lateral magnetic field, in this work, is possible due to the anti-parallel dipole coupling between the separated charges in the probe and the sample, which leads to the effective formation of a lateral magnetic dipole. Therefore, mapping of the lateral magnetic field distribution should be possible in any sample in which such charge separation can be induced, irrespective of the specific sample geometry. We are also optimistic to envisage, that this approach could be extended to propagating surface plasmon polariton waves as well [39]. From this point of view, we believe that our method can be considered as a complementary one to those already reported in the literature.

2.3 Conclusions

In conclusion, we have shown that the lateral magnetic near-field distribution of surface plasmon resonance modes in optical nanobar antennas can be visualized by means of aperture scanning near-field optical microscopy. The formation of an effective magnetic dipole between the hollow-pyramid probe and the antenna was shown to excite standing wave-like surface plasmons in the antenna, only at the SPR lateral magnetic field maxima. This excitation results in a measurable modulation of the transmitted light intensity. These findings are of paramount importance for achieving a complete characterization, including the magnetic field components, of electromagnetic near-field light phenomena mediated by nanoplasmonic devices.

Our findings suggest that aperture-SNOM can be considered as an important complement to the available scattering-SNOM techniques. It would, for example, be the method of choice for near-field studies of optical magnetic field enhancing and confining nanoantennas [25–27].

2.4 Methods

2.4.1 Sample Fabrication

The sample consists of a 150 μm thick glass slide coated with 10 nm of indium tin oxide (ITO) and a thin Ti adhesion layer (Fig. 2.7). A 50 nm thick gold film was sputtered and covered with another Ti adhesion layer and a negative tone hydrogen silsesquioxane (HSQ) resist. The nanostructures were further structured using electron beam lithography and Xe ion milling. The resulting bar width W is ∼70 nm.

A residual resist layer with an estimated thickness of 30 nm remains on top of the gold particles and is not removed. Optically, this layer behaves as silicon dioxide and causes the SPR modes to redshift (*e.g.*: 20 nm for the $l = 3$ mode of an $L = 1120$ nm antenna) due to the increase in surrounding refractive index. Additionally, the thickness of the layer will affect the spatial resolution [71] and the probe-sample coupling strength [63]. Although a detailed study of these effects for the present system was not performed, the results are expected to be qualitatively valid for a broad range of layer thicknesses. Most importantly, the layer serves as a dielectric insulator, preventing electrical contact, and therefore conductive coupling, between the nanoparticles and the metallic SNOM probe. This allows us to do fast contact mode scanning of the sample without drastically altering the plasmonic properties. The sample is organized in arrays, which consist of bars with increasing size in steps of 20, 30 or 50 nm.

2.4.2 FDTD Simulations

Simulations were performed with the commercial FDTD Maxwell equations solver Lumerical © [72]. For the near-field simulations, the nanostructure (including the resist layer on top of the metal), the hollow pyramid, and the substrate were placed in an 7 μm × 7 μm × 3.5 μm volume with perfectly matched layer (PML) boundaries and a mesh of 5 nm × 5 nm × 2.5 nm covering the nanostructure and the pyramid's aperture. For excitation, a plane wave source is positioned inside the pyramid.

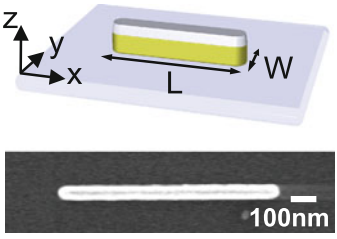

Fig. 2.7 Sketch of the sample structure and SEM image of a single nanobar of length $L = 1120$ nm and width $W = 70$ nm

To reproduce the experimental conditions as accurate as possible, the NA of the collection objective was taken into account by calculating the transmission intensity through a rectangular surface spanning the same collection angle. The permittivity of Au and Al was taken from Refs. [73, 74], respectively. The refractive index of the substrate and resist layer was set to $n = 1.4$. The ITO and Ti layers have a negligible effect on the results and this effect is not included in the simulations.

Field profiles in the absence of the probe were obtained using a point dipole source positioned above the edge of the bar in order to excite both odd and even order modes through phase retardation effects [57]. For the calculation of the plasmon dispersion in Fig. 2.6b the mode solver of Lumerical FDTD was used.

2.4.3 *Electric and Magnetic Field Profiles at the Apex of the Probe*

The structure of the probe was modelled following the information provided by the manufacturer (materials used, layer thicknesses, cone angle, and aperture size). Schematics of the simulated probe together with the dimensions is shown in Fig. 2.8a. Surface roughness, possible layer thickness variations, and rounding of the edges were not taken into account.

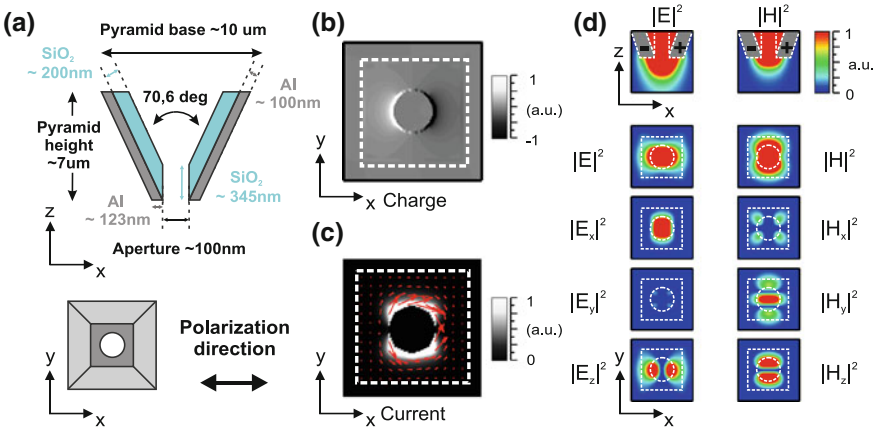

Fig. 2.8 Probe characterization. **a** Schematics of the simulated probe—*side view* (*top*) and *bottom view* (*bottom*). **b** Charge distribution inside the probe 30 nm above the aperture shows dipolar charge separation. **c** Current distribution inside the probe 30 nm above the probe aperture shows that the currents flow in two curved halfs of a *circle*. **d** Electric (*left*) and magnetic (*right*) field distributions at the probe aperture for an x-polarized incident plane wave at $\lambda = 1$ μm. x-z cross-sections taken through the probe center, x-y cross-sections 30 nm below the aperture. *Dashed white lines* indicate probe's boundaries

Finite-difference time-domain (FDTD) simulations of the probe, performed with Lumerical © [72], show that an incident x-polarized plane wave induces a dipolar charge polarization at its apex (Fig. 2.8b). The corresponding current profile (Fig. 2.8c), shows that the current flows following the red arrows. As a result, the H_y field is adding up just beneath the probe as is evident from the field profiles shown in Fig. 2.8d. The H_x and H_z fields produced by these currents are zero at a vertical plane through the middle of the probe, along the direction of incident light polarization. The electric and the magnetic field plots have a common color scale.

The profiles are obtained at $\lambda = 1\,\mu$m and remain almost unchanged throughout the experimental spectral range. For the field profiles, the x-z cross-sections are taken through the probe center and the x-y cross-sections 30 nm below the aperture. For the charge and current profiles, the x-y cross section is taken 30 nm above the aperture.

References

1. L. Novotny, N. van Hulst, Antennas for light. Nat. Photonics **5**, 83–90 (2011)
2. W.L. Barnes, A. Dereux, T.W. Ebbesen, Surface plasmon subwavelength optics. Nature **424**, 824–830 (2003)
3. V. Giannini, A.I. Fernandez-Domínguez, S.C. Heck, S.A. Maier, Plasmonic nanoantennas: fundamentals and their use in controlling the radiative properties of nanoemitters. Chem. Rev. **111**, 3888–3912 (2011)
4. S. Lal, S. Link, N.J. Halas, Nano-optics from sensing to waveguiding. Nat. Photonics **1**, 641–648 (2007)
5. R. Zia, J.A. Schuller, M.L. Brongersma, Near-field characterization of guided polariton propagation and cutoff in surface plasmon waveguides. Phys. Rev. B **74**, 165415 (2006)
6. V.K. Valev, D. Denkova, X. Zheng, A.I. Kuznetsov, C. Reinhardt, B.N. Chichkov, G. Tsutsumanova, E.J. Osley, V. Petkov, B. De Clercq, A.V. Silhanek, Y. Jeyaram, V. Volskiy, P.A. Warburton, G.A.E. Vandenbosch, S. Russev, O.A. Aktsipetrov, M. Ameloot, V.V. Moshchalkov, T. Verbiest, Plasmon-enhanced sub-wavelength laser ablation: plasmonic nanojets. Adv. Mater. **24**, OP29–OP35 (2012)
7. S.A. Maier, P.G. Kik, H.A. Atwater, S. Meltzer, E. Harel, B.E. Koel, A.A. Requicha, Local detection of eletromagnetic energy transport below the diffraction limit in metal nanoparticle plasmon waveguides. Nat. Mater. **2**, 229–232 (2003)
8. V.K. Valev, A.V. Silhanek, B. De Clercq, W. Gillijns, Y. Jeyaram, X. Zheng, V. Volskiy, O.A. Aktsipetrov, G.A.E. Vandenbosch, M. Ameloot, V.V. Moshchalkov, T. Verbiest, U-shaped switches for optical information processing at the nanoscale. Small **7**, 2573–2576 (2011)
9. D. Dregely, R. Taubert, J. Dorfmüller, R. Vogelgesang, K. Kern, H. Giessen, 3D optical Yagi-Uda nanoantenna array. Nat. Commun. **2**, 267 (2011)
10. K.F. MacDonald, N.I. Zheludev, Active plasmonics: current status. Laser Photonics Rev. **4**, 562–567 (2010)
11. L. Yin, V.K. Vlasko-Vlasov, J. Pearson, J.M. Hiller, J. Hua, U. Welp, D.E. Brown, C.W. Kimball, Subwavelength focusing and guiding of surface plasmons. Nano Lett. **5**, 1399–1402 (2005)
12. I.I. Smolyaninov, Two-dimensional plasmonic metamaterials. Appl. Phys. A **87**, 227–234 (2007)
13. V.M. Shalaev, Optical negative-index metamaterials. Nat. Photonics **1**, 41–48 (2007)
14. N.J. Halas, S. Lal, W.-S. Chang, S. Link, P. Nordlander, Plasmons in strongly coupled metallic nanostructures. Chem. Rev. **111**, 3913–3961 (2011)
15. N. Verellen, P. Van Dorpe, C. Huang, K. Lodewijks, G.A.E. Vandenbosch, L. Lagae, V.V. Moshchalkov, Plasmon line shaping using nanocrosses for high sensitivity localized surface plasmon resonance sensing. Nano Lett. **11**, 391–397 (2011)

16. M.E. Stewart, C.R. Anderton, L.B. Thompson, J. Maria, S.K. Gray, J.A. Rogers, R.G. Nuzzo, Nanostructured plasmonic sensors. Chem. Rev. **108**, 494–521 (2008)
17. A.V. Kabashin, P. Evans, S. Pastkovsky, W. Hendren, G.A. Wurtz, R. Atkinson, R. Pollard, V.A. Podolskiy, A.V. Zayats, Plasmonic nanorod metamaterials for biosensing. Nat. Mater. **8**, 867–871 (2009)
18. T. Chung, S.-Y. Lee, E.Y. Song, H. Chun, B. Lee, Plasmonic nanostructures for nano-scale bio-sensing. Sensors **11**, 10907–10929 (2011)
19. M.W. Knight, H. Sobhani, P. Nordlander, N.J. Halas, Photodetection with active optical antennas. Science **332**, 702 (2011)
20. P. Neutens, P. Van Dorpe, I. De Vlaminck, L. Lagae, G. Borghs, Electrical detection of confined gap plasmons in metal-insulator-metal waveguides. Nat. Photonics **3**, 283–286 (2009)
21. J. Zhou, T. Koschny, C.M. Soukoulis, Magnetic and electric excitations in split ring resonators. Opt. Express **15**, 17881–17890 (2007)
22. C.J. Tang, P. Zhan, Z.S. Cao, J. Pan, Z. Chen, Z.L. Wang, Magnetic field enhancement at optical frequencies through diffraction coupling of magnetic plasmon resonances in metamaterials. Phys. Rev. B **83**, 041402 (2011)
23. J.B. Pendry, D. Schurig, D.R. Smith, Controlling electromagnetic fields. Science **312**, 1780–1782 (2006)
24. C.M. Soukoulis, S. Linden, M. Wegener, Negative refractive index at optical wavelengths. Science **315**, 47–49 (2007)
25. T. Grosjean, M. Mivelle, F.I. Baida, G.W. Burr, U.C. Fischer, Diabolo nanoantenna for enhancing and confining the magnetic optical field. Nano Lett. **11**, 1009–1013 (2011)
26. Z. Gao, L. Shen, E. Li, L. Xu, Z. Wang, Cross-Diabolo nanoantenna for localizing and enhancing magnetic field with arbitrary polarization. J. Lightwave Technol. **30**, 829–833 (2012)
27. S. Koo, M.S. Kumar, J. Shin, D. Kim, N. Park, Extraordinary magnetic field enhancement with metallic nanowire: role of surface impedance in Babinet's principle for sub-skin-depth regime. Phys. Rev. Lett. **103**, 263901 (2009)
28. H. Giessen, R. Vogelgesang, Glimpsing the weak magnetic field of light. Science **326**, 529–530 (2009)
29. M. Burresi, D. van Oosten, T. Kampfrath, H. Schoenmaker, R. Heideman, A. Leinse, L. Kuipers, Probing the magnetic field of light at optical frequencies. Science **326**, 550–553 (2009)
30. H. Kihm, S. Koo, Q. Kim, K. Bao, J. Kihm, W. Bak, S. Eah, C. Lienau, H. Kim, P. Nordlander, N. Halas, N. Park, D.-S. Kim, Bethe-hole polarization analyser for the magnetic vector of light. Nat. Commun. **2**, 451 (2011)
31. M.W. Klein, C. Enkrich, M. Wegener, S. Linden, Second-harmonic generation from magnetic metamaterials. Science **313**, 502–504 (2006)
32. E. Abbe, Beiträge zur Theorie des Mikroskops und der mikroskopischen Wahrnehmung. Arch. Mikrosk. Anat. **9**, 413–468 (1873)
33. L. Rayleigh, On the theory of optical images with special reference to the optical microscope. Phil. Mag. **5**, 167–195 (1896)
34. E.J.R. Vesseur, R. de Waele, M. Kuttge, A. Polman, Direct observation of plasmonic modes in Au nanowires using high-resolution cathodoluminescence spectroscopy. Nano Lett. **7**, 2843–2846 (2007)
35. M. Bosman, V.J. Keast, M. Watanabe, A.I. Maaroof, M.B. Cortie, Mapping surface plasmons at the nanometre scale with an electron beam. Nanotechnology **18**, 165505 (2007)
36. P. Ghenuche, S. Cherukulappurath, T.H. Taminiau, N.F. van Hulst, R. Quidant, Spectroscopic mode mapping of resonant plasmon nanoantennas. Phys. Rev. Lett. **101**, 116805 (2008)
37. J. Dorfmüller, R. Vogelgesang, T.R. Weitz, C. Rockstuhl, C. Etrich, T. Pertsch, F. Lederer, K. Kern, Fabry-Pérot resonances in one-dimensional plasmonic nanostructures. Nano Lett. **9**, 2372–2377 (2009)
38. K. Imura, T. Nagahara, H. Okamoto, Near-field opticalimaging of plasmon modes in gold nanorods. J. Chem. Phys. **122**, 154701 (2005)
39. R. Zia, M.L. Brongersma, Surface plasmon polariton analogue to Young's double-slit experiment. Nat. Nanotechnol. **2**, 426–429 (2007)

40. E.H. Synge, A suggested model for extending microscopic resolution into the ultra-microscopic region. Phil. Mag. **6**, 356–362 (1928)
41. D.W. Pohl, W. Denk, M. Lanz, Optical stethoscopy: image recording with resolution $\lambda/20$. Appl. Phys. Lett. **44**, 651 (1984)
42. L. Novotny, S.J. Stranick, Near-field optical microscopy and spectroscopy with pointed probes. Annu. Rev. Phys. Chem. **57**, 303–331 (2006)
43. R. Esteban, R. Vogelgesang, J. Dorfmüller, A. Dmitriev, C. Rockstuhl, C. Etrich, K. Kern, Direct near-field optical imaging of higher order plasmonic resonances. Nano Lett. **8**, 3155–3159 (2008)
44. A. Dereux, C. Girard, J.-C. Weeber, Theoretical principles of near-field optical microscopies and spectroscopies. J. Chem. Phys. **112**, 7775 (2000)
45. G. Colas des Francs, C. Girard, J.-C. Weeber, A. Dereux, Relationship between scanning near-field optical images and local density of photonic states. Chem. Phys. Lett. **345**, 512–516 (2001)
46. E. Devaux, A. Dereux, E. Bourillot, J.-C. Weeber, Y. Lacroute, J.-P. Goudonnet, C. Girard, Local detection of the optical magnetic field in the near zone of dielectric samples. Phys. Rev. B **62**, 10504 (2000)
47. J.-S. Bouillard, S. Vilain, W. Dickson, A.V. Zayats, Hyperspectral imaging with scanning near-field optical microscopy: applications in plasmonics. Opt. Express **18**, 16513 (2010)
48. S.I. Bozhevolnyi, Near-field mapping of surface polariton fields. J. Microsc. **202**, 313–319 (2001)
49. L.D. Landau, E.M. Lifshitz, *Electrodynamics of Continuous Media* (Pergamon, Oxford, 1960)
50. R.L. Olmon, M. Rang, P.M. Krenz, B.A. Lail, L.V. Saraf, G.D. Boreman, M.B. Raschke, Determination of electric-field, magnetic-field, and electric-current distributions of infrared optical antennas: a near-field optical vector network analyzer. Phys. Rev. Lett. **105**, 167403 (2010)
51. T. Grosjean, I.A. Ibrahim, M.A. Suarez, G.W. Burr, M. Mivelle, D. Charraut, Full vectorial imaging of electromagnetic light at subwavelength scale. Opt. Express **18**, 5809–5824 (2010)
52. M. Seo, A.J.L. Adam, J.H. Kang, J. Lee, S.C. Jeoung, Q.H. Park, P.C.M. Planken, D.S. Kim, Fourier-transform terahertz near-field imaging of one-dimensional slit arrays: mapping of electric-field-, magnetic-field-, and poynting vectors. Opt. Express **15**, 11781 (2007)
53. A. Bitzer, H. Merbold, A. Thoman, T. Feurer, H. Helm, M. Walther, Terahertz near-field imaging of electric and magnetic resonances of a planar metamaterial. Opt. Express **17**, 3826–3834 (2009)
54. E. Verhagen, J.A. Dionne, L.K. Kuipers, H.A. Atwater, A. Polman, Near-field visualization of strongly confined surface plasmon polaritons in metal-insulator-metal waveguides. Nano Lett. **8**, 2925–2929 (2008)
55. M. Celebrano, M. Zavelani-Rossi, P. Biagioni, D. Polli, M. Finazzi,L. Duò, G. Cerullo, M. Labardi, M. Allegrini, J. Grand, P. Royer, and P.M. Adam, Mapping local field distribution at metal nanostructures by near-field second-harmonic generation. In: Proceedings of the SPIE, plasmonics: metallic nanostructures and their optical properties V 6641, 66411E–1 2007
56. Witec Wissenschaftliche Instrumente und Technologie GmbH (2014), http://www.witec.de
57. J. Dorfmüller, R. Vogelgesang, W. Khunsin, C. Rockstuhl, C. Etrich, K. Kern, Plasmonic nanowire antennas: experiment, simulation, and theory. Nano Lett. **10**, 3596–3603 (2010)
58. B. Hecht, B. Sick, U.P. Wild, V. Deckert, R. Zenobi, O.J.F. Martin, D.W. Pohl, Scanning near-field optical microscopy with aperture probes: fundamentals and applications. J. Chem. Phys. **112**, 7761–7774 (2000)
59. K. Imura, T. Nagahara, H. Okamoto, Characteristic near-field spectra of single gold nanoparticles. Chem. Phys. Lett. **400**, 500–505 (2004)
60. Y. Ekinci, A. Christ, M. Agio, O.J.F. Martin, H.H. Solak, J.F. Löffler, Electric and magnetic resonances in arrays of coupled gold nanoparticle in-tandem pairs. Opt. Express **16**, 13287 (2008)
61. A. Dmitriev, T. Pakizeh, M. Käll, D.S. Sutherland, Gold-silica-gold nanosandwiches: tunable bimodal plasmonic resonators. Small **3**, 294–299 (2007)

62. J.A. Porto, P. Johansson, S.P. Apell, T. López-Rios, Resonance shift effects in apertureless scanning near-field optical microscopy. Phys. Rev. B **67**, 085409 (2003)
63. A. García-Etxarri, I. Romero, J.F. García de Abajo, R. Hillenbrand, J. Aizpurua, Influence of the tip in near-field imaging of nanoparticle plasmonic modes: weak and strong coupling regimes. Phys. Rev. B **79**, 125439 (2009)
64. G. Schider, J.R. Krenn, A. Hohenau, H. Ditlbacher, A. Leitner, F.R. Aussenegg, W.L. Schaich, I. Puscasu, B. Monacelli, G. Boreman, Plasmon dispersion relation of Au and Ag nanowires. Phys. Rev. B **68**, 155427 (2003)
65. L. Novotny, Effective wavelength scaling for opticalantennas. Phys. Rev. Lett. **98**, 266802 (2007)
66. F. Neubrech, D. Weber, R. Lovrincic, A. Pucci, M. Lopes, T. Toury, M. Lamy de la Chapelle, Resonances of individual lithographic gold nanowires in the infrared. Appl. Phys. Lett. **93**, 163105 (2008)
67. R.L. Olmon, P.M. Krenz, A.C. Jones, G.D. Boreman, M.B. Raschke, Near-field imaging of optical antenna modes in the mid-infrared. Opt. Express **16**, 20295 (2008)
68. S. Vignolini, F. Intonti, F. Riboli, L. Balet, L.H. Li, M. Francardi, A. Gerardino, A. Fiore, D.S. Wiersma, M. Gurioli, Magnetic imaging in photonic crystal microcavities. Phys. Rev. Lett. **105**, 123902 (2010)
69. M. Burresi, T. Kampfrath, D. van Oosten, J.C. Prangsma, B.S. Song, S. Noda, L. Kuipers, Magnetic light-matter interactions in a photonic crystal nanocavity. Phys. Rev. Lett. **105**, 123901 (2010)
70. M. Celebrano, P. Biagioni, M. Zavelani-Rossi, D. Polli, M. Labardi, M. Allegrini, M. Finazzi, L. Duò, G. Cerullo, Hollow-pyramid based scanning near-field optical microscope coupled to femtosecond pulses: a tool for nonlinear optics at the nanoscale. Rev. Sci. Instrum. **80**, 033704 (2009)
71. X. Heng, X. Cui, D.W. Knapp, J. Wu, Z. Yaqoob, E.J. McDowell, D. Psaltis, C. Yang, Characterization of light collection through a subwavelength aperture from a point source. Opt. Express **14**, 10410–10425 (2006)
72. Lumerical Solutions (2014), http://www.lumerical.com
73. P.B. Johnson, R.W. Christy, Optical constants of thenoble metals. Phys. Rev. B **6**, 4370–4379 (1972)
74. D.R. Lide, *CRC Handbook of Chemistry and Physics*, 3rd edn. (CRC, Boca Raton, 2000)

http://www.springer.com/978-3-319-28792-8

Optical Characterization of Plasmonic Nanostructures: Near-Field Imaging of the Magnetic Field of Light

Denkova, D.

2016, XXVI, 88 p. 36 illus., 35 illus. in color., Hardcover
ISBN: 978-3-319-28792-8